

# Computational homogenization of the debonding of particle reinforced composites: The role of interphases in interfaces



Daniel W. Spring<sup>a</sup>, Glaucio H. Paulino<sup>a,b,\*</sup>

<sup>a</sup> Department of Civil and Environmental Engineering, University of Illinois at Urbana-Champaign, Urbana, IL, United States

<sup>b</sup> School of Civil and Environmental Engineering, Georgia Institute of Technology, Atlanta, GA, United States

## ARTICLE INFO

### Article history:

Received 31 March 2015

Received in revised form 1 July 2015

Accepted 7 July 2015

### Keywords:

Representative unit cells

Interphases

Interfacial debonding

Coupled cohesive–friction relation

## ABSTRACT

There are four primary factors which influence the macroscopic constitutive response of particle reinforced composites: component properties, component concentrations, interphases, and interfacial debonding. Interphases are often a byproduct of surface treatments applied to the particles to control agglomeration. Alternatively, in polymer based materials such as carbon-black reinforced rubber, an interphase or “bound rubber” phase often occurs at the particle–matrix interface. This interphasial region has been known to exist for many decades, but is often omitted in computational investigations of such composites. In this paper, we present an investigation into the influence of interphases on the large deformation response of particle reinforced composites. In addition, since particles tend to debond from the matrix at large deformations, we investigate the influence of interfacial debonding on the macroscopic constitutive response. The investigation considers two different microstructures; both a simplified single particle model, and a more complex polydisperse representative unit cell. Cohesive elements, which follow the Park–Paulino–Roesler traction–separation relation, are inserted between each particle and its corresponding interphase to account for debonding. To account for friction, we present a new, coupled cohesive–friction model and detail its formulation and implementation. For each microstructure, we discuss the influence of the interphase thickness and stiffness on the global constitutive response in both uniaxial tension and simple shear. To validate the computational framework, comparisons are made with experimental results available in the literature.

© 2015 Elsevier B.V. All rights reserved.

## 1. Introduction

The macroscopic response of particle reinforced composites is influenced by not only the component properties and component concentrations, but also the interfacial interaction between the particles and the matrix. In particular, the inclusion of stiff particles to a soft matrix can lead to an increase in composite stiffness, strength, impact resistance, and abrasion resistance [1,2]. Additionally, at large deformations particles tend to debond from the matrix, influencing both the ductility and fracture toughness of the composite [3–5]. To enhance or control these properties, the particles themselves can be tailored through surface treatments [6–8]. Often, surface treatments are applied to the particles of a composite material to meet various desired specifications. For instance, these treatments are often employed to reduce residual

tensile stresses between the particles and the matrix or to reduce particle agglomeration [7,9]. On the other hand, as a result of chemical interactions, an interphase may form between the particle and the matrix during manufacturing and processing. Even though these interphases are typically microscopic, they can greatly influence the macroscopic behavior of composite materials. The extent and composition of this interphase depends on a number of factors, including the surface area and surface treatment of the particles, as well as the level of mixing and age of the composite [1].

Recent experiments by Qu et al. [10,11], used atomic force microscopy to conduct in situ imaging of particle–elastomer interactions. They demonstrated that the macroscopic properties (in particular, the stiffness and scratch resistance) of the composite can be tailored, by selectively designing the surface chemistry of the particles. Ramier et al. [6,8] investigated the influence of different surface treatments on the large deformation response of silica particle reinforced styrene butadiene rubber. They conducted a series of experiments on consistently prepared specimens, but applied a different surface treatment to the particles in each

\* Corresponding author at: School of Civil and Environmental Engineering, Georgia Institute of Technology, Atlanta, GA, United States.

E-mail addresses: [spring2@illinois.edu](mailto:spring2@illinois.edu) (D.W. Spring), [paulino@gatech.edu](mailto:paulino@gatech.edu) (G.H. Paulino).

sample. Their investigation focused on the influence of the cross-linking that occurs in the matrix as a result of the different surface treatments, and concluded that the applied surface treatment on the particles is often the primary factor controlling the macroscopic constitutive response of the composite. Moreover, at large deformations, they observed the particles debonding from the matrix. Debonding is characterized by a localized region of failure (or interfacial debonding) that accumulates around the particle inclusions. There have been numerous experimental investigations demonstrating the interfacial debonding behavior of particles under large deformations; some examples of which are illustrated in Fig. 1.

In contrast to the numerous experimental investigations, there have been few theoretical investigations which consider the effect of either interphases or interfacial debonding in the finite deformation regime. One of the few formulations for debonding under finite strains was presented by Brassart et al. [16]. They extend the Mori–Tanaka homogenization scheme [17] to account for the debonding of composite materials under finite strains; however, they only consider hydrostatic loading in three-dimensions and do not account for the presence of interphases. More recently, Goudarzi et al. [18] presented a theoretical framework capable of describing the influence of interphases on the macroscopic constitutive response of particle reinforced elastomers. They compare their formulation to both numerical and experimental results [6], and found excellent correlation with both. However, their investigation focuses on the influence of perfectly bonded interphases, excluding the consideration of interfacial debonding. To the best of the author's knowledge, there has been no theoretical formulation presented which accounts for both interphases and interfacial debonding under finite deformations.

There are four primary factors which influence the macroscopic constitutive response of particle reinforced composites: component properties, component concentrations, interphases, and interfacial debonding. This paper presents a computational framework capable of capturing the influence of interphases and interfacial debonding on the finite deformation response of particle reinforced composites. The influence of the thickness and modulus of the interphase is considered, and debonding is accounted for

through the use of cohesive elements. The remainder of the paper is organized as follows. In Section 2, we discuss some related numerical investigations using the cohesive element method for interfacial debonding. Section 3 discusses the computational framework for this investigation. Section 4 presents a new, coupled cohesive–friction relation and details its formulation and implementation. Both single particle and multi-particle periodic microstructures are considered in this paper. The results for the single particle microstructure are presented in Section 5.1, and those for the multi-particle microstructure are presented in Section 5.2. We validate the computational framework by challenging it with experimental data in Section 6. Finally, some conclusions, and potential extensions are discussed in Section 7.

## 2. Related work

The numerical investigation of interfacial debonding using the cohesive element method was pioneered by Needleman in 1987 [19]. In his investigation, *intrinsic* cohesive elements were used to capture the full range of particle debonding behavior, from void nucleation to full decohesion. Intrinsic cohesive elements are inserted along the boundary of a particle, with zero initial thickness, and transmit normal and shear tractions to the surrounding bulk elements. The magnitude of the tractions depends on the separation of the elements and the selected traction–separation relation. There have been many traction–separation relations which have seen widespread use; including linear, bilinear, trapezoidal, polynomial, and exponential softening relations. A discussion of many of the prevalent traction–separation relations may be found in the review paper by Park and Paulino [20].

To date, most investigations of interfacial debonding have been conducted using two-dimensional and simplified three-dimensional models. In two dimensions, the plain strain assumption is often employed to model fiber inclusions. Zhong and Knauss [21,22] used linear softening cohesive elements to investigate debonding in fiber-reinforced composites with structured microstructures. They focused on the tensile response of the composites, and studied the influence of various factors; including particle size, shape and distribution. Moraleda et al. [23] used a

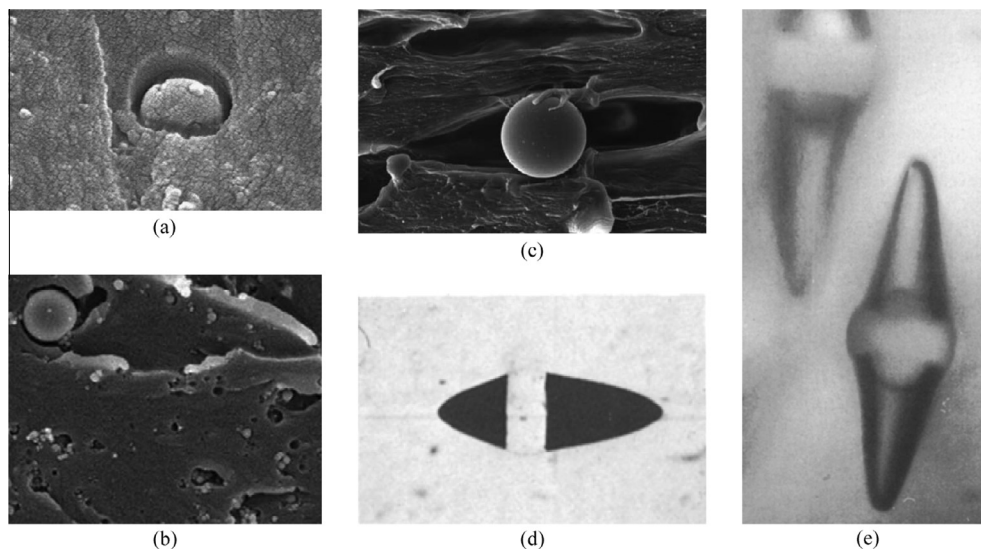


**Fig. 1.** Experimentally observed debonding behavior of particle reinforced composites under large deformations. (a) Debonding of aluminum oxide particles from an epoxy resin (extracted from Wetzel et al. [12]). (b) Multiple locations of silane treated alumina particles debonding from an epoxy matrix (mse.rpi.edu). (c) A glass particle surrounded by the void created due to deformation of the polypropylene/glass composite (extracted from Thio et al. [13]). The glass particles in this investigation were treated using heptadecafluorodecyl trichlorosilane. (d) Glass beads, treated with ethylsilane, debonding from natural rubber (extracted from Gent and Park [14]). (e) Large void creation around glass particles in a high-density polyethylene matrix (extracted from Zhuk et al. [15]).

linear softening cohesive relation to study the influence of interfacial debonding on the tensile response of fiber-reinforced elastomers. They considered both a single particle microstructure and a microstructure with a random distribution of monodisperse particles. Inglis et al. [24] used two-dimensional models to investigate debonding in polydisperse microstructures containing a high concentration of particulates. Brassart et al. [16] used the same numerical framework as Inglis et al. to capture the debonding of rigid inclusions under axisymmetric tension. They considered periodic unit cells with a random distribution of up to ten monodisperse particles.

To accurately capture the effect of spherical particle inclusions, fully three-dimensional modeling is necessary. Matouš and Geubelle [25,26] used an effective displacement, exponential softening, cohesive relation to study the debonding of spherical particles. In their fully three-dimensional investigation, they considered both a single particle microstructure and a four-particle microstructure. In their investigation of the four-particle microstructure, they used a slight perturbation in the position of the particles. Through these simplified microstructures they were able to demonstrate the significant influence of interfacial debonding on the macroscopic constitutive response of these composites.

One common feature among all of the investigations mentioned above is that none of them consider the influence of interphases. While it has been shown experimentally that interphases significantly alter the macroscopic response of particle reinforced composites, their inclusion in computational models is widely omitted. This publication aims to take a first look at the combination of interphases and interfacial debonding in particle reinforced composites undergoing finite deformations, and to motivate the inclusion of interphases in future investigations.

### 3. Computational framework

In this paper, we develop a fully three-dimensional computational framework capable of capturing the influence of interphases and interfacial debonding on the finite deformation response of particle reinforced composites. We consider both a single particle microstructure, and a multi-particle microstructure; and, for the most generality, in the multi-particle microstructure we consider a random distribution of polydisperse particles. The single particle microstructure is presented to illustrate the local behavior during progressive debonding. While this model is simplified, it can provide insight into the important characteristics, and provide guidance into tailoring the design of particle-reinforced composite materials. The multi-particle microstructure, however, is more representative of a real material.

#### 3.1. Single particle microstructure

The single particle model replicates the case of a perfectly repeating, structured microstructure. The model considers a single particle placed at the centroid of a cube. The particle is assumed to be numerically rigid [27], and we assume that a compliant interphase forms around the surface of the particle. The particle is assumed to be spherical, and the interphase thickness is assumed to be uniform, as illustrated in Fig. 2(a). The geometry is discretized with quadratic tetrahedral elements using the automatic mesh generator Netgen [28]. A sample mesh for the particle and interphase is illustrated in Fig. 2(b).

#### 3.2. Multi-particle microstructure

In the multi-particle model, we consider a random distribution of particles. These models, often referred to as representative unit

cells (RUCs), are commonly used to represent realistic microstructures [29,30]. In our investigation, the RUC is selected to be a cube of unit side  $L = 1$ . For the most generality, we consider the particles to be polydisperse, represented through three families of particle sizes [27]. The particle locations are generated using a constrained adsorption algorithm [31,27,18]. The procedure we use to generate the polydisperse microstructures is as follows:

- Families of particles with three different radii,  $r_p^{(i)}$  ( $i = 1, 2, 3$ ), are selected with concentrations  $c^{(i)}$ , surrounded by interphases with thickness  $t^{(i)}$ , such that:

$$\left\{ r_p^{(1)}, r_p^{(2)}, r_p^{(3)} \right\} \cong \left\{ r_p, \frac{7}{9}r_p, \frac{4}{9}r_p \right\} \quad \text{with} \quad r_p = L \left( \frac{3c^{(1)}}{4\pi N_p} \right)^{1/3}, \quad (1)$$

$$\left\{ c^{(1)}, c^{(2)}, c^{(3)} \right\} = \{0.5c, 0.25c, 0.25c\} \quad \text{with} \quad c^{(1)} + c^{(2)} + c^{(3)} = c, \quad (2)$$

$$\left\{ \frac{t^{(1)}}{r_p^{(1)}}, \frac{t^{(2)}}{r_p^{(2)}}, \frac{t^{(3)}}{r_p^{(3)}} \right\} = \left\{ \frac{t}{r_p}, \frac{t}{r_p}, \frac{t}{r_p} \right\} \quad \text{with} \quad t = \gamma r_p, \quad (3)$$

where  $N_p$  denotes the number of particles with the largest radius and thickest interphase, and  $\gamma$  is a constant multiplier.

- The particles are added sequentially, from the family with the largest particle size to that with the smallest particle size. To ensure an adequate spatial discretization, each placement of a particle is constrained such that the following conditions are met:
  - The center-to-center distance between a newly placed particle and any previously accepted one must exceed the minimum value  $s_1 = 2(1 + d_1)(r_p^{(i)} + t^{(i)})$ , where the offset distance is fixed as  $d_1 \geq 0.05$ . In compact notation, and to ensure the generation of a periodic microstructure (discussed further in Section 3.3), this constraint takes the form:

$$\left\| \mathbf{X}^j - \mathbf{X}^k - \mathbf{h} \right\| \geq s_1, \quad (4)$$

where  $j, k = 1, 2, \dots, N$ ,  $\mathbf{X}^j$  ( $\mathbf{X}^k$ ) denotes the location of the centroid of particle  $j$  ( $k$ ),  $N$  is the total number of particles in the microstructure, and  $\mathbf{h}$  is a vector composed of 0,  $L$ , and  $-L$  entries for each Cartesian component.

- The distance between the boundary of the RUC and the surface of any interphase should exceed a minimum value  $s_2 = d_2(r_p^{(i)} + t^{(i)})$  where the offset distance is fixed as  $d_2 = 0.05$ . In compact notation, this constraint is represented by the inequalities:

$$\left| X_l^j - r_p^{(i)} - t^{(i)} \right| \geq s_2, \quad \left| X_l^j + r_p^{(i)} + t^{(i)} - L \right| \geq s_2, \quad (l = 1, 2, 3). \quad (5)$$

In this investigation, we set  $N_p = 10$  such that the RUC contains a total of 80 particles [18]. Figs. 3 and 4 illustrate sample RUCs, generated using the above procedure, for particle concentrations of  $c = 0.1$  and  $c = 0.2$ , respectively.

A mesh refinement study was conducted using randomly generated meshes with approximately 100,000, 200,000 and 300,000 quadratic tetrahedral elements, as illustrated in Fig. 5. Meshes with approximately 200,000 elements displayed a sufficient level of accuracy, and is the target mesh size for the results presented in the remainder of the paper.

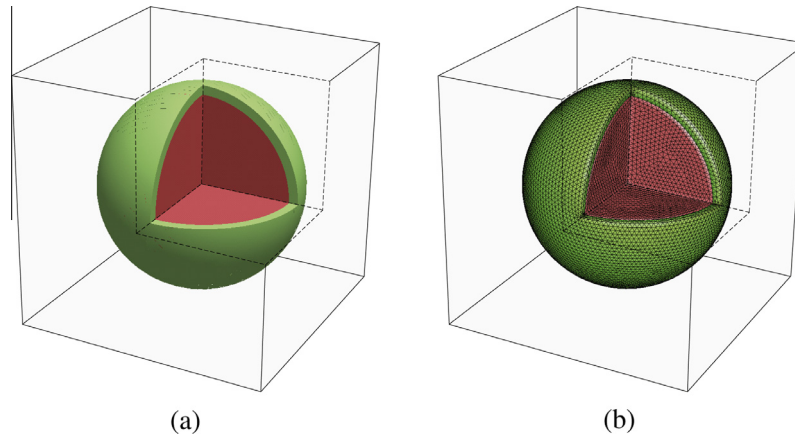


**Fig. 2.** The single particle model: (a) geometry and (b) sample mesh used for the particle and interphase. Note that the mesh for the bulk matrix is excluded from the figure for illustrative purposes only. Additionally, an octant of the geometry is removed to illustrate the particle and interphase.

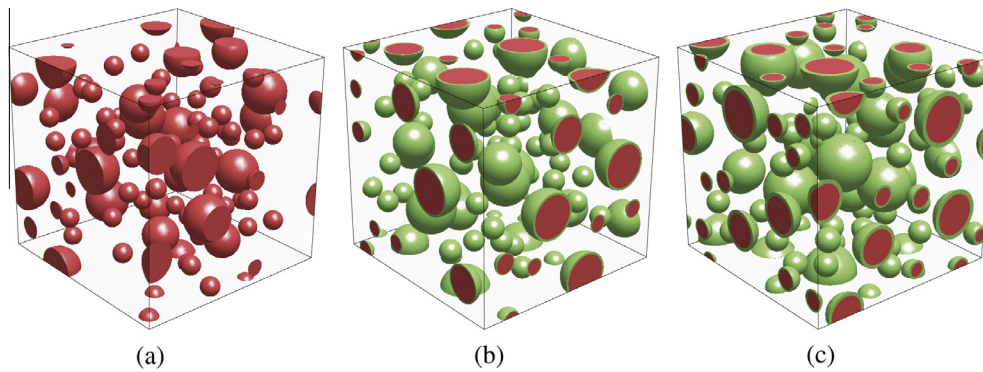


**Fig. 3.** Representative polydisperse microstructures, containing a random distribution of 80 particles of three different radii. The particles constitute a concentration of  $c = 0.1$  and are surrounded by (a) no interphase, (b) interphases with a thickness of  $t = 0.1r_p^{(i)}$ , and (c) interphases with a thickness of  $t = 0.2r_p^{(i)}$ .

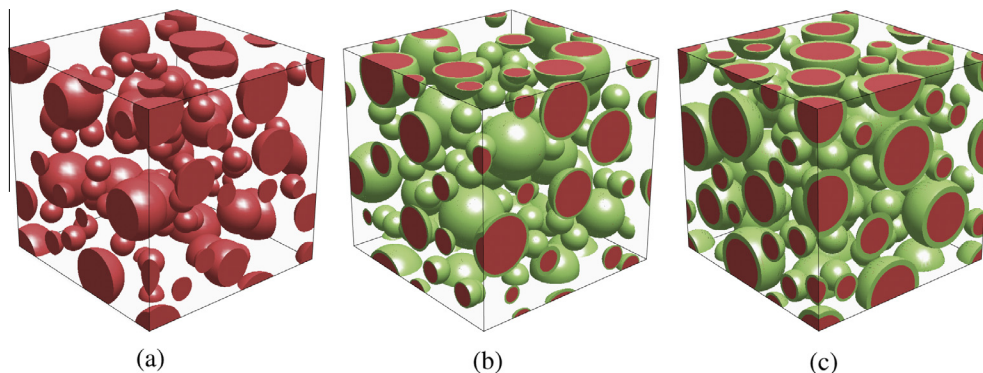


**Fig. 4.** Representative polydisperse microstructures, containing a random distribution of 80 particles of three different radii. The particles constitute a concentration of  $c = 0.2$  and are surrounded by (a) no interphase, (b) interphases with a thickness of  $t = 0.1r_p^{(i)}$ , and (c) interphases with a thickness of  $t = 0.2r_p^{(i)}$ .

### 3.3. Periodic boundary conditions

To capture the behavior of a truly periodic microstructure, the model considers both a periodic geometry (see Fig. 6) and periodic boundary conditions. The periodic boundary conditions are expressed as:

$$\begin{aligned} u_k(0, X_2, X_3) - u_k(L, X_2, X_3) &= (\bar{F}_{k1} - \delta_{k1})L, \\ u_k(X_1, 0, X_3) - u_k(X_1, L, X_3) &= (\bar{F}_{k2} - \delta_{k2})L, \\ u_k(X_1, X_2, 0) - u_k(X_1, X_2, L) &= (\bar{F}_{k3} - \delta_{k3})L, \end{aligned} \quad (6)$$

where  $X_1$ ,  $X_2$  and  $X_3$  correspond to a Cartesian frame of reference, where the origin is placed at a corner of the cell and the axes are aligned with the edges of the cell. Moreover,  $k$  is a constant ( $=1, 2, 3$ ),  $\delta_{ki}$  denotes the Kronecker delta, and  $\bar{F}_{ki}$  are the components of the prescribed average deformation gradient. To impose these periodic boundary conditions, the surface mesh on opposite faces of the cell need to be mirrors of one another. The pairing of the nodes on opposite faces is conducted automatically by Netgen [28], and incorporated into the Abaqus analysis using multi-point constraints [32].

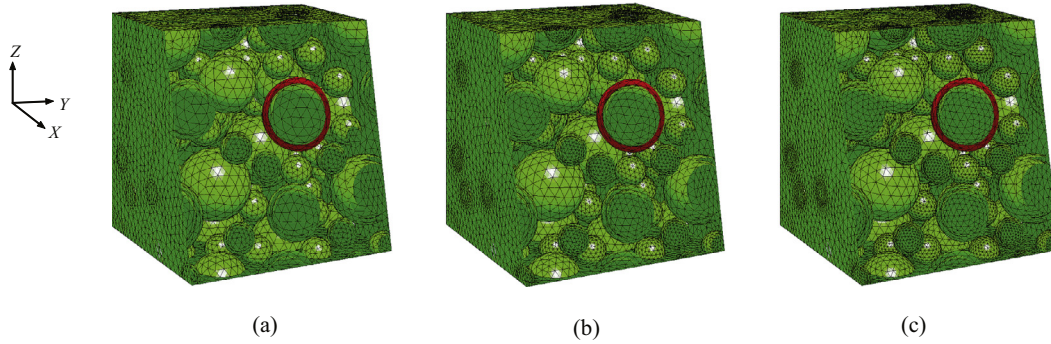


**Fig. 5.** Three representative meshes in the undeformed configuration for a distribution of polydisperse particles with a concentration of  $c = 0.2$ , and an interphase thickness of  $t = 0.2r_p^{(i)}$ : (a) a coarse mesh with approximately 100,000 elements, (b) a fine mesh with approximately 200,000 elements, and (c) a very fine mesh with approximately 300,000 elements.

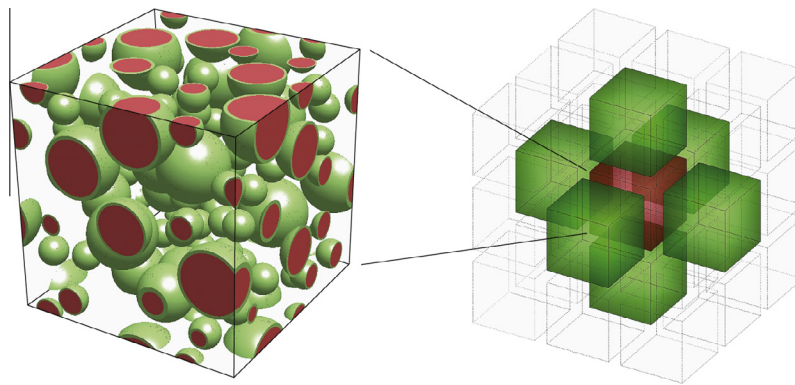


**Fig. 6.** Depiction of a periodic geometry. Periodicity ensures that the particles are placed in such a manner that if the cell were to be replicated and placed adjacent, in any of the three ( $\pm$ ) Cartesian directions, it would result in a continuous microstructure.

### 3.4. Assessment of isotropy

In all models containing a finite number of randomly placed particles, the isotropy of the microstructure is only approximate [27]. There are multiple approaches for determining whether the random placement of particles results in an approximately isotropic microstructure. Many authors take a geometric approach, computing the centroid or moment of inertia of the particles [31,33,34]. Alternatively, one could take a constitutive approach, by examining the co-axiality between the stress and strain tensors [27,18]. In an isotropic material, the average Cauchy stress tensor,  $\bar{\sigma} = \overline{\mathbf{S}\mathbf{F}^T}$  and average left Green-Cauchy strain tensor  $\bar{\mathbf{B}} = \overline{\mathbf{F}\mathbf{F}^T}$  are co-axial, and the angle between their principal axes (the angle of co-axiality) is zero. Since the constitutive approach is sufficient, it is the method we choose to assess the isotropy of our microstructures. Each microstructure is tested, and those which result in an angle of co-axiality greater than 0.05 radians are discarded [27,18]. We use this approach for all loading conditions, particle concentrations and interphase thicknesses considered in this investigation.

## 4. Accounting for interfacial debonding

To account for interfacial debonding, cohesive elements are inserted between each particle and its surrounding interphase, as illustrated in Fig. 7. The cohesive elements initially have zero thickness, and, as the elements separate, they transfer normal and shear tractions to the surrounding bulk elements. There have been numerous traction–separation relations proposed in the literature, see for example the relations proposed by Xu and Needleman [35]

and Ortiz and Pandolfi [36]. The traction–separation relation used in this investigation follows the Park–Paulino–Roesler (PPR) cohesive model [37]. The PPR model is potential-based, is consistent, contains physically based input parameters, and satisfies all boundary conditions associated with fracture [37]. Typically, potential-based models do not account for either unloading/reloading, contact, or frictional relations within the model. Here, we will briefly detail the PPR softening model and the unloading/reloading relation chosen in this work. In addition, we will present a new frictional relation which is compatible with, and coupled to, the PPR formulation.

### 4.1. Cohesive traction–separation relation

The cohesive elements are inserted into the model prior to the start of the simulation, thus, the traction–separation relation follows the intrinsic PPR cohesive model. The details of PPR model have been extensively documented, so only the pertinent details are included here; extended details may be found in the principal publication [37]. The intrinsic model is implemented into the commercial software Abaqus through a user supplied subroutine [32,38]. The softening relations of the PPR model are derived from the following potential function:

$$\begin{aligned} \Psi(\Delta_n, \Delta_t) = & \min(\phi_n, \phi_t) \\ & + \left[ \Gamma_n \left( 1 - \frac{\Delta_n}{\delta_n} \right)^\alpha \left( \frac{m}{\alpha} + \frac{\Delta_n}{\delta_n} \right)^m + \langle \phi_n - \phi_t \rangle \right] \\ & \times \left[ \Gamma_t \left( 1 - \frac{|\Delta_t|}{\delta_t} \right)^\beta \left( \frac{n}{\beta} + \frac{|\Delta_t|}{\delta_t} \right)^n + \langle \phi_t - \phi_n \rangle \right], \end{aligned} \quad (7)$$

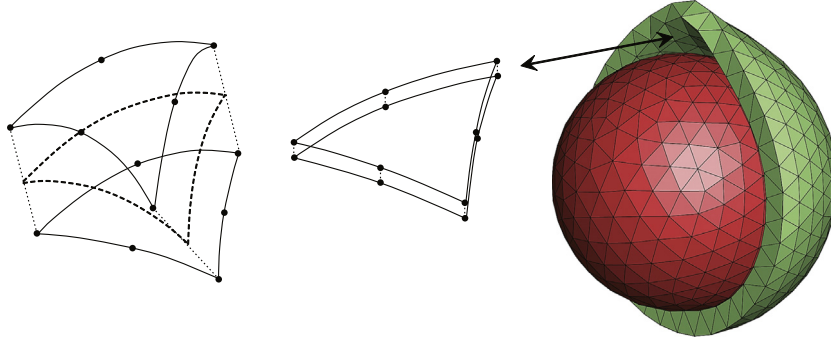


Fig. 7. Cohesive elements with zero initial thickness are inserted between each particle and its corresponding interphase.

where  $\Delta_n$  and  $\Delta_t$  are the normal and tangential crack opening widths, respectively. Moreover,  $\phi_n$  and  $\phi_t$  correspond to the normal and tangential fracture energies. The parameters  $\alpha$  and  $\beta$  control the shape of the softening relation. The softening relation is approximately linear if the shape parameters are equal to 2. If they are less than 2, or greater than 2, the shape of the softening relation will be concave or convex, respectively. The potential function is defined over a domain of dependence; which is bounded by the normal final crack opening ( $\delta_n$ ) and the tangential final crack opening ( $\delta_t$ ):

$$\begin{aligned}\delta_n &= \frac{\phi_n}{\sigma_{\max}} \alpha \lambda_n (1 - \lambda_n)^{\alpha-1} \left(\frac{\alpha}{m} + 1\right) \left(\frac{\alpha}{m} \lambda_n + 1\right)^{m-1}, \\ \delta_t &= \frac{\phi_t}{\tau_{\max}} \beta \lambda_t (1 - \lambda_t)^{\beta-1} \left(\frac{\beta}{n} + 1\right) \left(\frac{\beta}{n} \lambda_t + 1\right)^{n-1}.\end{aligned}\quad (8)$$

where  $\sigma_{\max}$  and  $\tau_{\max}$  correspond to the normal and tangential cohesive strengths, respectively.

The normal and tangential cohesive tractions are computed by taking the derivative of the potential with respect to the normal and tangential crack opening widths:

$$\begin{aligned}T_n(\Delta_n, \Delta_t) &= \frac{\partial \Psi}{\partial \Delta_n} \\ &= \frac{\Gamma_n}{\delta_n} \left[ m \left(1 - \frac{\Delta_n}{\delta_n}\right)^\alpha \left(\frac{m}{\alpha} + \frac{\Delta_n}{\delta_n}\right)^{m-1} - \alpha \left(1 - \frac{\Delta_n}{\delta_n}\right)^{\alpha-1} \left(\frac{m}{\alpha} + \frac{\Delta_n}{\delta_n}\right)^m \right] \\ &\quad \times \left[ \Gamma_t \left(1 - \frac{|\Delta_t|}{\delta_t}\right)^\beta \left(\frac{n}{\beta} + \frac{|\Delta_t|}{\delta_t}\right)^n + \langle \phi_t - \phi_n \rangle \right],\end{aligned}\quad (9)$$

$$\begin{aligned}T_t(\Delta_n, \Delta_t) &= \frac{\partial \Psi}{\partial \Delta_t} \\ &= \frac{\Gamma_t}{\delta_t} \left[ n \left(1 - \frac{|\Delta_t|}{\delta_t}\right)^\beta \left(\frac{n}{\beta} + \frac{|\Delta_t|}{\delta_t}\right)^{n-1} - \beta \left(1 - \frac{|\Delta_t|}{\delta_t}\right)^{\beta-1} \left(\frac{n}{\beta} + \frac{|\Delta_t|}{\delta_t}\right)^n \right] \\ &\quad \times \left[ \Gamma_n \left(1 - \frac{\Delta_n}{\delta_n}\right)^\alpha \left(\frac{m}{\alpha} + \frac{\Delta_n}{\delta_n}\right)^m + \langle \phi_n - \phi_t \rangle \right] \frac{\Delta_t}{|\Delta_t|}.\end{aligned}\quad (10)$$

The energy constants  $\Gamma_n$  and  $\Gamma_t$  are related to the normal and tangential fracture energies. When the normal and tangential fracture energies are different ( $\phi_n \neq \phi_t$ ), the energy constants become:

$$\Gamma_n = (-\phi_n)^{(\phi_n - \phi_t)/(\phi_n - \phi_t)} \left(\frac{\alpha}{m}\right)^m, \quad \Gamma_t = (-\phi_t)^{(\phi_t - \phi_n)/(\phi_t - \phi_n)} \left(\frac{\beta}{n}\right)^n.\quad (11)$$

When the normal and tangential fracture energies are equal ( $\phi_n = \phi_t$ ), the energy constants simplify to:

$$\Gamma_n = -\phi \left(\frac{\alpha}{m}\right)^m, \quad \Gamma_t = \left(\frac{\beta}{n}\right)^n,\quad (12)$$

where the non-dimensional exponents,  $m$  and  $n$ , are evaluated from the shape parameters ( $\alpha, \beta$ ) and initial slope indicators ( $\lambda_n, \lambda_t$ ):

$$m = \frac{\alpha(\alpha-1)\lambda_n^2}{(1-\alpha\lambda_n^2)}, \quad n = \frac{\beta(\beta-1)\lambda_t^2}{(1-\beta\lambda_t^2)}.\quad (13)$$

Sample traction–separation relations are illustrated in Fig. 8.

#### 4.2. Unloading/reloading relation

The unloading/reloading relation used in this model is uncoupled, in the sense that unloading in the normal direction is viewed as independent of that in the tangential direction. The unloading relation is activated when the normal or tangential separation is past the peak cohesive strength of the element, and effects both the traction vector and the tangent matrix. The unloading/reloading relation in the model is linear to the origin [39,40], as illustrated in Fig. 9. The details of the implementation are not listed here, however, they are published elsewhere [38].

#### 4.3. Frictional relation

When a particle is in contact with its surrounding interphase, compressive and frictional forces ( $T_f$ ) are generated. Since the potential-based cohesive formulation does not explicitly account for a contact relation, we have chosen to use a simplified penalty approach to contact. As an element is distorted into an adjacent element the resisting force increases linearly in accordance with a corresponding stiffness. The modulus of this stiffness is chosen to correspond to a multiple of the slope of the cohesive hardening curve as it approaches zero opening displacement. Alternatively, other contact formulations could be used, such as the ones found in references [41,42].

There have been multiple techniques proposed for coupling a friction relation to a cohesive model. One of the first approaches can be attributed to Tvergaard [43]. In this approach, the onset of friction is assumed to occur only after the cohesive model has completely softened. Later authors revised this assumption, setting the onset of friction to occur at the onset of irreversible damage [42,44–46]. The main feature of this revised approach is that no frictional energy is dissipated prior to the onset of decohesion. Here, we outline a new mixed-mode frictional relation that, when coupled with the PPR cohesive model, presents a smooth transition from a cohesive zone to a pure frictional contact zone. In particular, the coupled frictional force is computed as:

$$T_f = \mu_f \kappa(\Delta_t) |T_n| \quad \text{when } T_n < 0 \quad \text{and } \Delta_t > \lambda_t \delta_t,\quad (14)$$

where  $\mu_f$  is the coefficient of friction, and  $\kappa(\Delta_t)$  may be thought of as a damage-type parameter, varying monotonically between 0 and 1 (when  $\Delta_t > \lambda_t \delta_t$ ). The relation chosen for  $\kappa$  is expressed as:

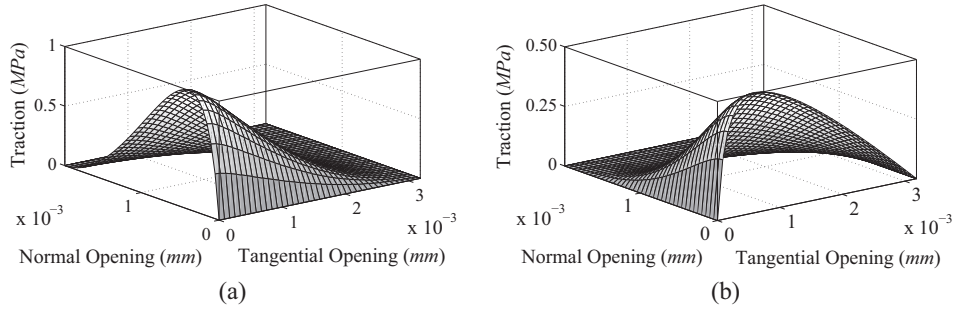


**Fig. 8.** Depiction of the traction–separation relation for the PPR model in the (a) normal direction and (b) tangential direction. Cohesive parameters:  $\phi_n = \phi_t = 1.0 \text{ N/m}$ ,  $\sigma_{\max} = 1.0 \text{ MPa}$ ,  $\tau_{\max} = 0.5 \text{ MPa}$ ,  $\alpha = 3$ ,  $\beta = 2$ ,  $\lambda_n = \lambda_t = 0.2$ .

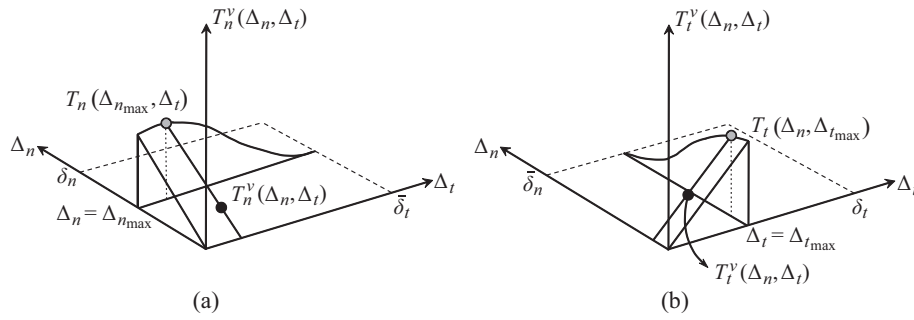


**Fig. 9.** Depiction of the uncoupled linear unloading/reloading relations for loading in the (a) normal direction and (b) tangential direction.

$$\kappa(\Delta_t) = \left(1 - \frac{T_t(0, \Delta_t)}{D_0 \Delta_t}\right)^s, \quad (15)$$

where  $s$  is an input parameter which controls the rate of transition between cohesive and frictional forces. The influence of  $s$  on  $\kappa$  is illustrated in Fig. 10(a). Moreover,  $T_t(0, \Delta_t)$  is the tangential cohesive traction computed at zero normal opening displacement, and  $D_0$  is the stiffness at the onset of damage (see Fig. 10(b)) calculated as:

$$D_0 = \frac{\Gamma_t}{\delta_t} \left[ n(1 - \lambda_t)^\beta \left(\frac{n}{\beta} + \lambda_t\right)^{n-1} - \beta(1 - \lambda_t)^{\beta-1} \left(\frac{n}{\beta} + \lambda_t\right)^n \right] \times \left[ \Gamma_n \left(\frac{m}{\alpha}\right)^m + \langle \phi_n - \phi_t \rangle \right] \frac{1}{\lambda_t \delta_t}, \quad (16)$$

where the input parameters  $\Gamma_t$ ,  $\Gamma_n$ ,  $\delta_t$ ,  $\delta_n$ ,  $n$ ,  $m$ ,  $\alpha$ ,  $\beta$ , and  $\lambda_t$  are the same as those in the PPR cohesive model.

The frictional force vector is coupled to the cohesive force vector through the following relation:

$$\mathbf{T} = \left\{ \begin{array}{l} T_n \\ T_t \frac{\Delta_2}{\Delta_t} + T_f \left( \frac{|\Delta_2|}{|\Delta_2|} \right) \frac{\dot{\Delta}_2}{|\dot{\Delta}_2|} \\ T_t \frac{\Delta_3}{\Delta_t} + T_f \left( \frac{|\Delta_3|}{|\Delta_3|} \right) \frac{\dot{\Delta}_3}{|\dot{\Delta}_3|} \end{array} \right\}, \quad (17)$$

where  $\Delta_2$  and  $\Delta_3$  correspond to crack opening widths in the tangential plane of fracture, and the  $(\cdot)$  operator represents the change in the crack opening width. The tangential crack opening width,  $\Delta_t$ , is coupled through the relation  $\Delta_t = \sqrt{\Delta_2^2 + \Delta_3^2}$ . The material tangent matrix for this constitutive model is included in Appendix A. A sample cohesive–friction relation is plotted versus the coupled tangential crack opening width in Fig. 10(b). From the figure it is clear that frictional forces initiate at the onset of cohesive softening (irreversible damage), and that the transition from softening behavior

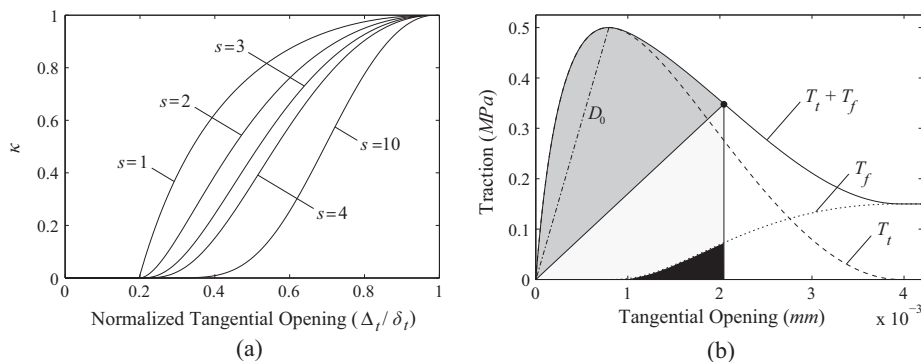


**Fig. 10.** (a) Influence of the value of  $s$  on the damage variable,  $\kappa(\Delta_t)$ , as per Eq. (15). (b) Tangential traction, including friction ( $\Delta_n < 0$ ,  $\lambda_t = 0.2$ , and  $s = 3$ ). The various energies at a given state are depicted: dark gray is the energy dissipated during the process of decohesion, light gray is the stored elastic energy, and black is the energy dissipated by friction.

to frictional behavior is monotonic and smooth. To illustrate the fully coupled, three-dimensional friction relation, the tangential components of the force vector (Eq. (17)) are decoupled then superimposed in Fig. 11.

The hysteretic response of the coupled cohesive–friction relation is illustrated in Fig. 12. Initially, the loading follows the cohesive relation; however, beyond the peak stress, frictional forces are generated and energy dissipation due to friction accumulates. As unloading occurs, the direction dependent frictional force generates a jump in the traction. When the cohesive element has fully separated (i.e. the cohesive force goes to zero), only frictional forces are generated.

## 5. Results and discussion

We now apply the above computational framework to several examples with various microstructural configurations. First, we investigate the single particle model, then present results for full field simulations on representative unit cells. In each configuration, we examine the influence of interphase thickness and stiffness on the macroscopic constitutive response in both uniaxial and shear loading. There are various stored-energy functions available for

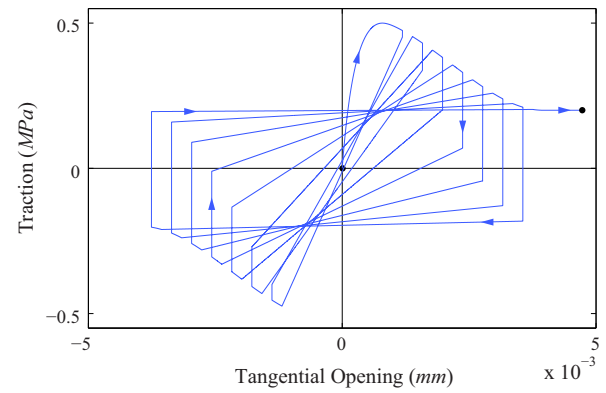


**Fig. 12.** Tangential traction versus tangential opening during cyclic loading ( $\Delta_n < 0$ ,  $s = 3$  and  $\mu = 0.5$ ).

representing the behavior of hyperelastic materials [47], however the most commonly applied may be the neo-Hookean model. In this section, the matrix material is assumed to be an incompressible neo-Hookean rubber, with stored-energy function:

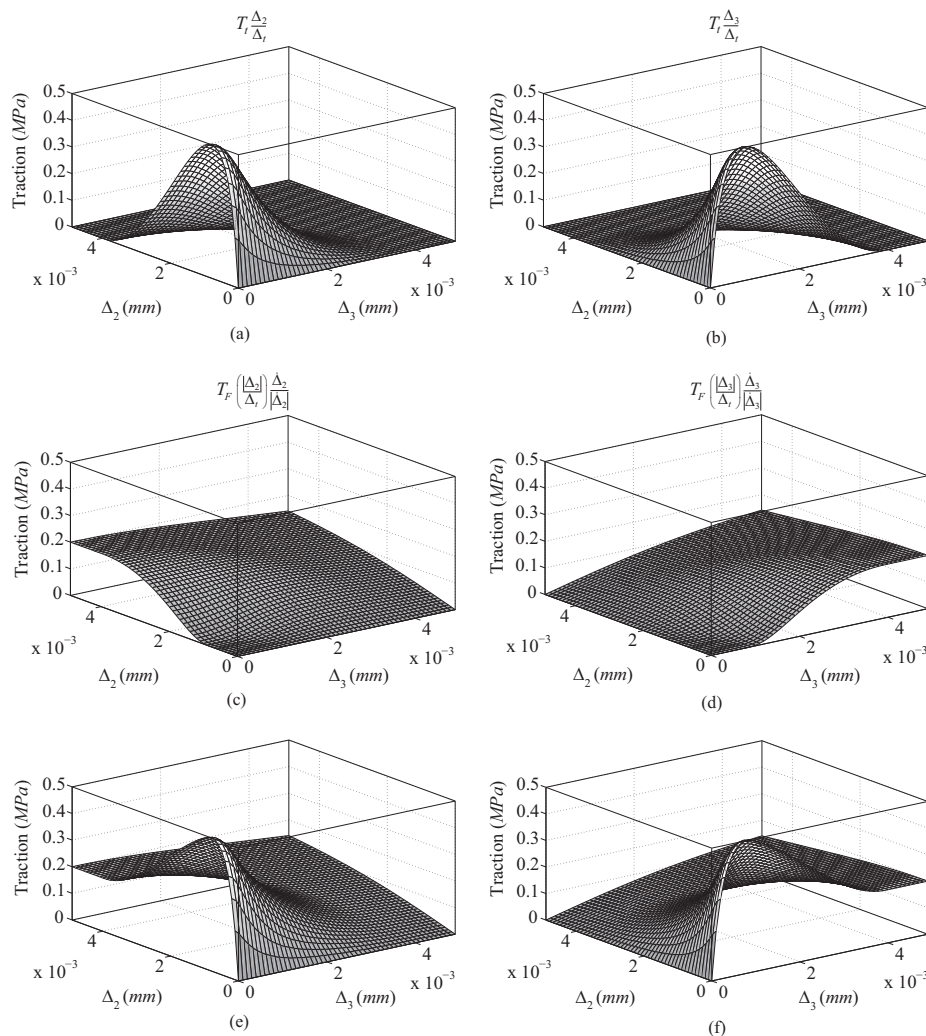


**Fig. 11.** Visual decomposition of the three-dimensional, coupled cohesive–friction model: (a) cohesive traction in the  $\Delta_2$  direction; (b) cohesive traction in the  $\Delta_3$  direction; (c) friction traction in the  $\Delta_2$  direction; (d) friction traction in the  $\Delta_3$  direction; (e) coupled cohesive–friction traction in the  $\Delta_2$  direction; and (f) coupled cohesive–friction traction in the  $\Delta_3$  direction. The cohesive and friction parameters are:  $\alpha = \beta = 3$ ,  $\lambda_n = \lambda_t = 0.2$ ,  $\phi_n = \phi_t = 1.0$  N/m,  $\sigma_{\max} = \tau_{\max} = 0.5$  MPa,  $s = 3$ ,  $\mu = 0.5$ , and  $T_n = -0.4$  MPa; and it is assumed that  $\Delta_2$  and  $\Delta_3 > 0$ .

$$W = \frac{\mu}{2}[I_1 - 3], \quad (18)$$

where  $\mu$  is the initial shear modulus,  $I_1 = \mathbf{F} \cdot \mathbf{F}$  is the first principal invariant of the right Cauchy–Green tensor, and  $\mathbf{F}$  is the deformation gradient. The matrix is assumed to have an initial shear modulus,  $\mu_m$ , of 1.0 MPa, and the interphase surrounding each particle is assumed to have a modulus,  $\mu_i$ , which is a multiple of that in the bulk. The particles are assumed to have a modulus that is four orders of magnitude greater than that in the matrix ( $\mu_p = 10^4 \mu_m$ ), to numerically approximate the case of rigid particle inclusions [48,34]. In each case, the cohesive parameters are set as  $\sigma_{\max} = 0.5$  MPa,  $\phi = 1.0$  N/m,  $\alpha = 3$ , and  $\lambda = 0.2$ . For contact between the interphases and the rigid particles, the coefficient of friction is set at  $\mu_f = 1.0$  and the rate of transition between cohesive and friction forces is set at  $s = 3$ , in Eq. (15). The macroscopic strain is defined as  $\epsilon = h/H - 1$ , where  $h$  is the deformed length in the direction of loading, and  $H$  is the undeformed length of the edge of the cell. The macroscopic stress corresponds to the first Piola–Kirchhoff stress, measured as the force calculated in the deformed configuration applied over the undeformed surface of the model.

### 5.1. Single particle results

First, we consider the single particle model, and investigate the influence of the interphase thickness and stiffness on the macroscopic constitutive response in both uniaxial tension and simple shear. We consider the case of microparticle inclusions, with an assumed particle diameter of 10  $\mu\text{m}$ , and size the model based on the particle diameter and volume fraction. Thus, the cell dimensions for a particle concentration of  $c = 0.1$  and  $c = 0.2$  are  $17.4 \times 17.4 \times 17.4 \mu\text{m}$  and  $13.8 \times 13.8 \times 13.8 \mu\text{m}$ , respectively. The objective of this investigation is to demonstrate the ability of the computational framework to capture the complex decohesion process along the particle–interphase interface.

#### 5.1.1. Uniaxial tension

In uniaxial tension, progressive debonding occurs. Decohesion initiates at the poles of the particle, in the direction of loading, and propagates towards the equator. Upon decohesion, compressive regions are formed in the plane perpendicular to the axis of loading; due to the volume preserving nature of the matrix material. The void and compressive regions can be seen in the contour plots of principal stress, as illustrated in the deformed configuration in Fig. 13. In the matrix, a band of stress is concentrated at the location of the particle. The stress distribution in the interphase is illustrated in Fig. 13(b). The shape of the interphase coincides with the shape of the void. Contact between the interphase and the particle can be seen by the outward bulge in the deformed shape of the interphase. At the poles of the interphase, zero stress is observed, indicating a complete loss of load bearing capacity, or complete debonding of the particle. At the equator of the interphase, high contact stresses are distributed through a thick band in the interphase. The resulting stress distribution in the particle is illustrated in Fig. 13(c). As expected, the stress in the particle is concentrated in the band that remains in contact with the interphase, and the particle carries zero stress in the fully debonded regions.

The macroscopic constitutive response in uniaxial tension is plotted in Fig. 14. We illustrate cases for particle concentrations of  $c = 0.1$  and  $c = 0.2$ , and interphase thickness to particle radius ratios of  $t/r_p = 0.1$  and  $t/r_p = 0.2$ . The thicker and stiffer the interphase, the greater the influence on the constitutive response. For the case with a small particle concentration ( $c = 0.1$ ) and interphase thickness ( $t/r_p = 0.1$ ), the influence is the smallest, but is still significant. For example, when we consider the case with an

interphase stiffness of  $\mu_i = 10\mu_m = 10$  MPa (a similar modulus to that observed experimentally [10]), at a strain of 0.4 the global response is approximately 25% greater than in the case when no interphase is considered, as illustrated in Fig. 14(a). For the larger particle concentration,  $c = 0.2$ , the global response is approximately 115% greater than that without considering interphases, as illustrated in Fig. 14(c).

#### 5.1.2. Simple shear

The second loading condition we consider is simple shear. In this case, we observe a higher area of contact between the particle and the surrounding interphase in the deformed configuration. Thus, we expect the frictional forces in this scenario to be more significant; we will discuss and quantify this further in Section 5.2.1. The contour plots of principal stress for the matrix, interphase and particle are illustrated in Fig. 15. In the direction perpendicular to the plane of shear, the stress in the interphase is lower than that in the plane of shear. Additionally, the void region is concentrated into a smaller zone than in the uniaxial tension case, as demonstrated by the deformed shape of the interphase in Fig. 15(b). Because of the small void region, there remains a significant surface area of contact between the particle and the interphase, as demonstrated by the distribution of stress in the particle in Fig. 15(c).

The macroscopic constitutive response in simple shear is illustrated in Fig. 16. Similar to the case in uniaxial tension, we illustrate cases for particle concentrations of  $c = 0.1$  and  $c = 0.2$ , and interphase thickness to particle radius ratios of  $t/r_p = 0.1$  and  $t/r_p = 0.2$ . In simple shear, the influence of the interphase is noticeably less than in the case of uniaxial tension; however, the interphase continues to significantly alter the macroscopic constitutive response. For example, when we consider the case with a small particle concentration in Fig. 16(a), and an interphase stiffness of  $\mu_i = 10\mu_m$ , at a strain of 0.4 the global response is approximately 18% greater than in the case when no interphase is considered. The influence of the interphase is magnified as the particle concentration, and thus the effective concentration of the interphase, increases, as illustrated in Fig. 16(b) and (c).

### 5.2. Full representative unit cell results

Here we consider the case of more realistic microstructures, based on the full field simulations of polydisperse representative unit cells. The particle diameter is assumed to be 10  $\mu\text{m}$  for the largest family of particles, and the RUCs are sized based on the particle diameter and concentration. Thus, the cell dimensions for a particle concentration of  $c = 0.1$  and  $c = 0.2$  are  $47.1 \times 47.1 \times 47.1 \mu\text{m}$  and  $37.4 \times 37.4 \times 37.4 \mu\text{m}$ , respectively. First, we investigate the influence of frictional forces on the constitutive response of various microstructures, then demonstrate the influence of the interphase thickness and modulus in both uniaxial tension and simple shear loading.

#### 5.2.1. Influence of friction

To investigate the influence of frictional forces, we compare the full field results with and without friction, as illustrated in Fig. 17. As in the case with a single particle, we consider both uniaxial tension and simple shear loading, with various particle concentrations,  $c$ , and interphase thickness to particle radius ratios,  $t/r_p$ . In the case of uniaxial tension, the frictional forces are shown to impart little effect on the macroscopic constitutive response of the composite, as illustrated in Fig. 17(a). The inclusion of a frictional relation in the cohesive element formulation causes a slight increase in the effective stiffness of the composite, but, for the concentration and number of particles we have considered, it is

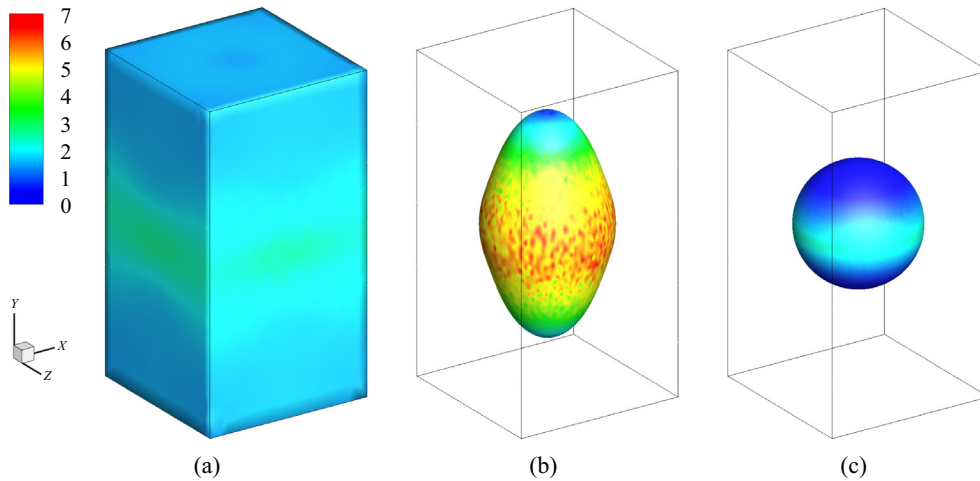


Fig. 13. Contour plot of principal stress in uniaxial tension in the (a) matrix, (b) interphase, and (c) particle, for the single particle model.

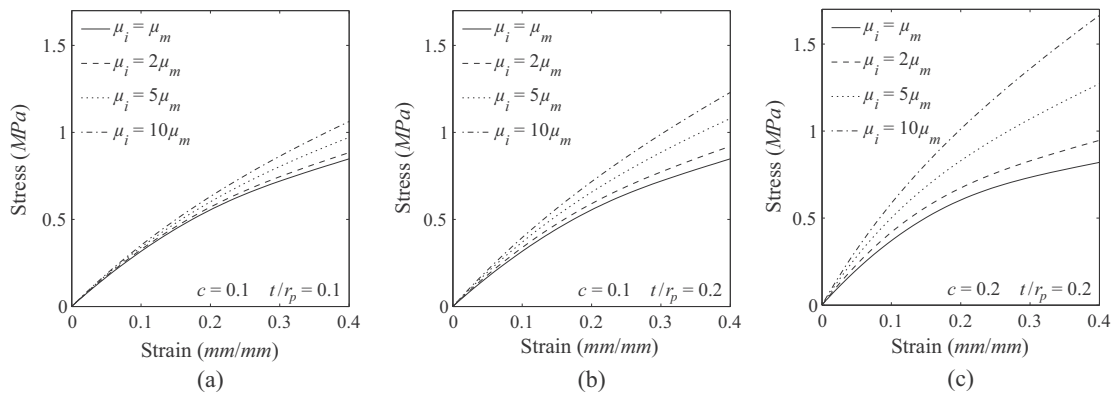


Fig. 14. Macroscopic constitutive response in uniaxial tension for microstructures with: (a)  $c = 0.1$  and  $t/r_p = 0.1$ ; (b)  $c = 0.1$  and  $t/r_p = 0.2$ ; and (c)  $c = 0.2$  and  $t/r_p = 0.2$ .

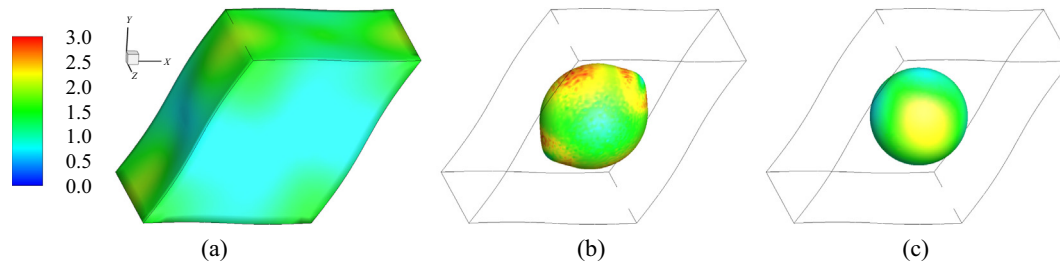


Fig. 15. Contour plot of principal stress in simple shear in the (a) matrix, (b) interphase, and (c) particle, for the single particle model.

negligible. It is valuable to note that the magnitude of frictional forces is dependent on the number of particles used to capture the respective concentration, thus, if a greater number of particles were used, the magnitude would increase. However, the underlying cause of the low influence will not change, as will be discussed in the next section. In the case of simple shear, the frictional forces are shown to have a greater influence on the composite's constitutive response, as illustrated in Fig. 17(b). This is expected behavior, since, in the previous investigation in the single particle model, we demonstrated that a large area of contact exists between the particle and the interphase in simple shear. This large area of contact generates large frictional forces.

We have demonstrated that the particle reinforced composite materials under investigation in this paper demonstrate a small influence of friction, however, there are alternate applications

wherein frictional forces are significant. In order to further verify and validate the newly proposed coupled cohesive–friction model presented in Section 4.3, we have included a supplementary example in Appendix B which demonstrates a significant dependence on friction.

### 5.2.2. Uniaxial tension

In uniaxial tension, a representative deformed microstructure is illustrated in Fig. 18(a). Each particle debonds from the surrounding matrix, as seen both in the deformed shape and in the contour plots in Fig. 18(b) and (c). Similar to the study on the single particle model, each particle is compressed by the surrounding matrix in a plane perpendicular to the direction of loading. The fully debonded regions alleviate the stress at the poles of the particles. The width of the small band of compression in the particles is indicative of the

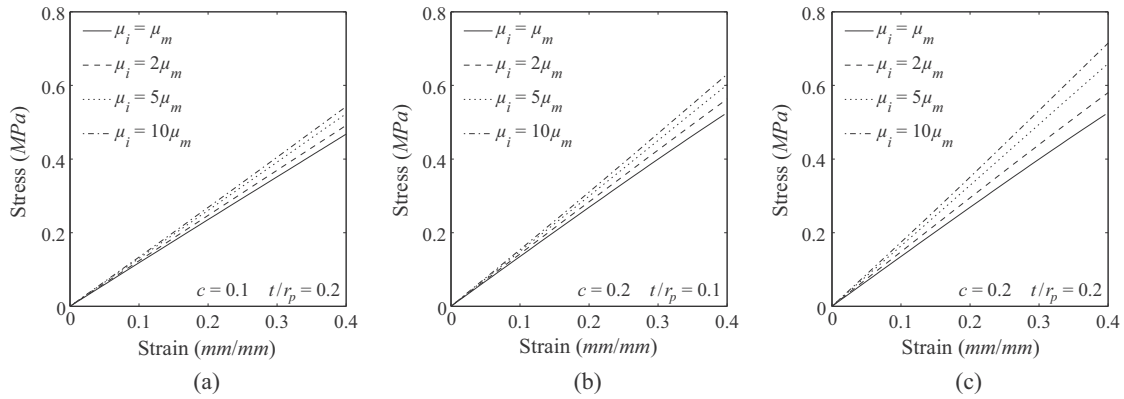


Fig. 16. Macroscopic constitutive response in simple shear for microstructures with: (a)  $c = 0.1$  and  $t/r_p = 0.2$ ; (b)  $c = 0.2$  and  $t/r_p = 0.1$ ; and (c)  $c = 0.2$  and  $t/r_p = 0.2$ .

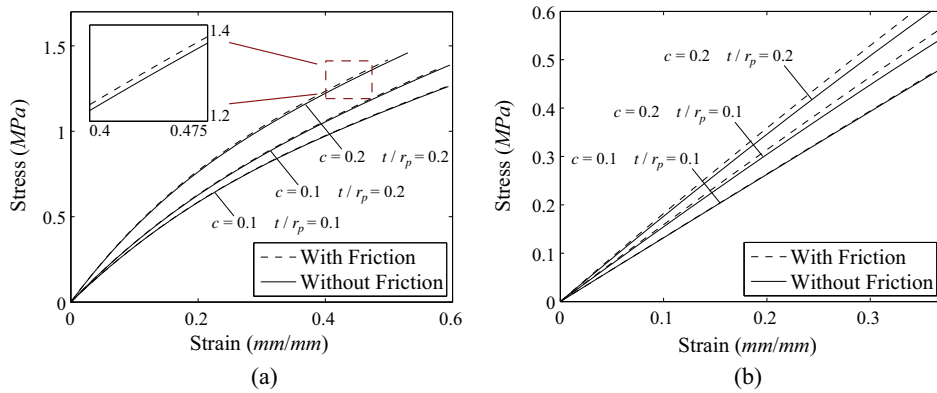


Fig. 17. Influence of friction on the global constitutive response of RUCs in (a) uniaxial tension, and (b) simple shear.

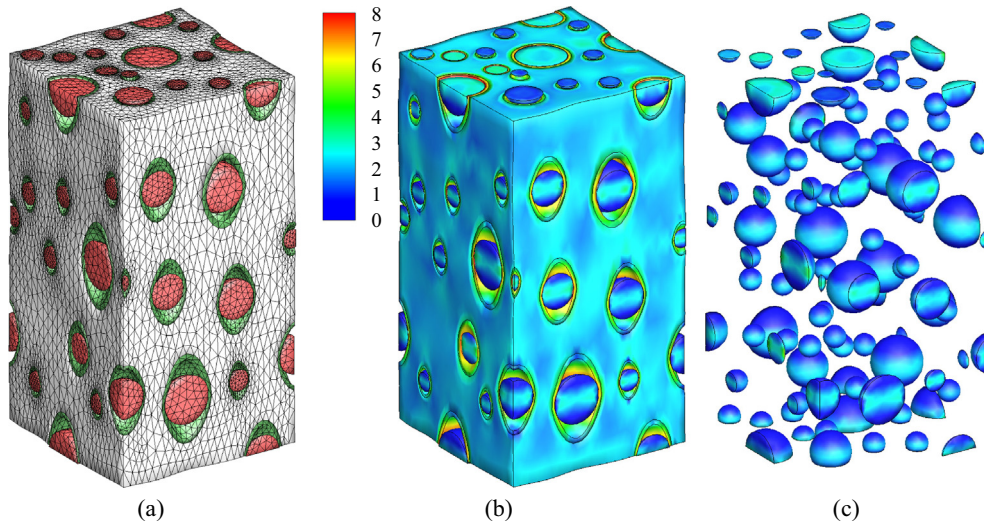


Fig. 18. (a) Deformed geometry of a representative unit cell with a particle concentration of  $c = 0.1$  and an interphase to particle radius ratio of  $t/r_p = 0.2$ , loaded in uniaxial tension. Contour plot of principal stress in uniaxial tension in the (b) entire model, and (c) particles.

small area of contact wherein frictional forces can be generated, explaining the small influence of friction on the global response seen in Fig. 17(a).

The macroscopic constitutive response in uniaxial tension is plotted in Fig. 19. We consider particle concentrations of  $c = 0.1$  and  $c = 0.2$ , and interphase thickness to particle radius ratios of

$t/r_p = 0.1$  and  $t/r_p = 0.2$ , and compare them to the response when no interphase is present. Because each microstructure is generated randomly, the response illustrated is an average of three simulations. As expected, the thicker and stiffer the interphase, the greater the influence on the constitutive response. Additionally, as is commonly noted in the literature [25], the large particles tend

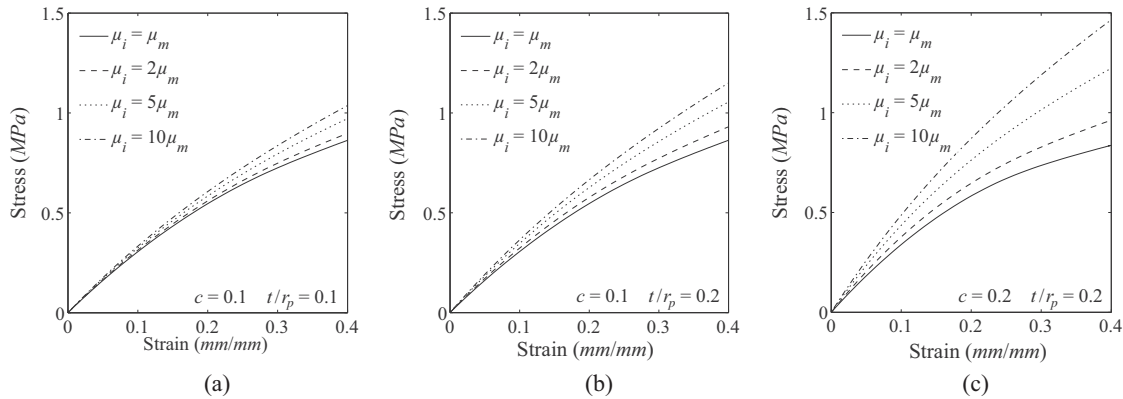


Fig. 19. Macroscopic constitutive response in uniaxial tension for microstructures with: (a)  $c = 0.1$  and  $t/r_p = 0.1$ ; (b)  $c = 0.1$  and  $t/r_p = 0.2$ ; and (c)  $c = 0.2$  and  $t/r_p = 0.2$ .

to debond from the matrix prior to the smaller particles fully debonding.

Even in the case with a small particle concentration ( $c = 0.1$ ) and interphase thickness ( $t/r_p = 0.1$ ), the interphase has a significant influence on the global response at relatively low strains. For example, at a strain of 0.4, microstructures with an interphase stiffness of  $\mu_i = 10\mu_m$  produce a global response which is approximately 25% greater than in the case when no interphase is considered, as illustrated in Fig. 19(a). For the larger particle concentration,  $c = 0.2$ , the global response is approximately 80% greater than that without considering interphases, as illustrated in Fig. 19(c).

### 5.2.3. Simple shear

In simple shear, a representative deformed microstructure is illustrated in Fig. 20(a). The zone of debonding around each particle is much smaller than that in uniaxial tension. Similar to the previous example, we also illustrate the stress contours in the particles in Fig. 20(b). As with the single particle model, the stress in the particles remains high at large strains; which explains the higher contribution of friction to the global response, as discussed in Section 5.2.1.

The macroscopic constitutive response in simple shear, for various microstructural configurations, is illustrated in Fig. 21. Similar to the study on the single particle model, in simple shear, the influence of the interphase is noticeably less than in the case of uniaxial tension; however, the interphase continues to significantly alter the macroscopic response. For the case with a small particle concentration in Fig. 21(a), and an interphase stiffness of  $\mu_i = 10\mu_m$ , at a strain of 0.4 the global response is approximately 20% greater

than in the case when no interphase is considered. For the case with a larger particle concentration and interphase thickness in Fig. 21(c), at a strain of 0.4, the global response is approximately 45% greater than in the case when no interphase is considered.

In summary, this series of numerical investigations clearly demonstrates that the inclusion of physically significant, microscopic interphases can dramatically alter the macroscopic constitutive response of particle reinforced composites. We are also able to demonstrate that frictional effects are negligible in tension induced debonding. By demonstrating that the presence of interphases and interfacial debonding significantly alters the macroscopic constitutive response of these composite materials, we hope to motivate the inclusion of such interphases in future investigations which model such composites.

## 6. Experimental validation

In this section, we verify that the proposed computational framework is capable of capturing representative experimental results from the literature. There are few experimental investigations which report all the necessary microscale and macroscale properties of the composite material, thus we make reasonable assumptions, and discuss them, where necessary. The experimental results selected for this comparison were reported in a series of papers by Yatsuyanagi et al. [9] and Suzuki et al. [7]. Their results correspond to a well-dispersed distribution of roughly spherical aggregates of silica particles in a styrene-butadiene rubber matrix. In their investigation, they study the influence of rubber/filler interaction, due to variations in coupling agents used in

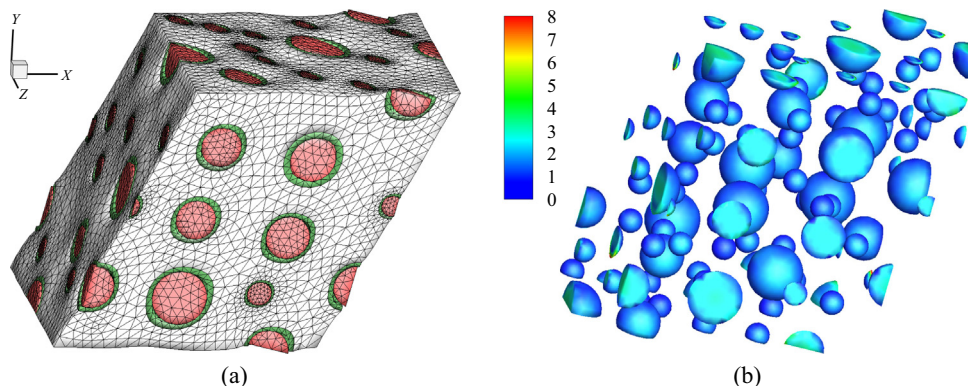


Fig. 20. (a) Deformed geometry of a representative unit cell with a particle concentration of  $c = 0.1$  and an interphase to particle radius ratio of  $t/r_p = 0.2$ , loaded in simple shear. (b) Contour plot of principal stress in the particles.

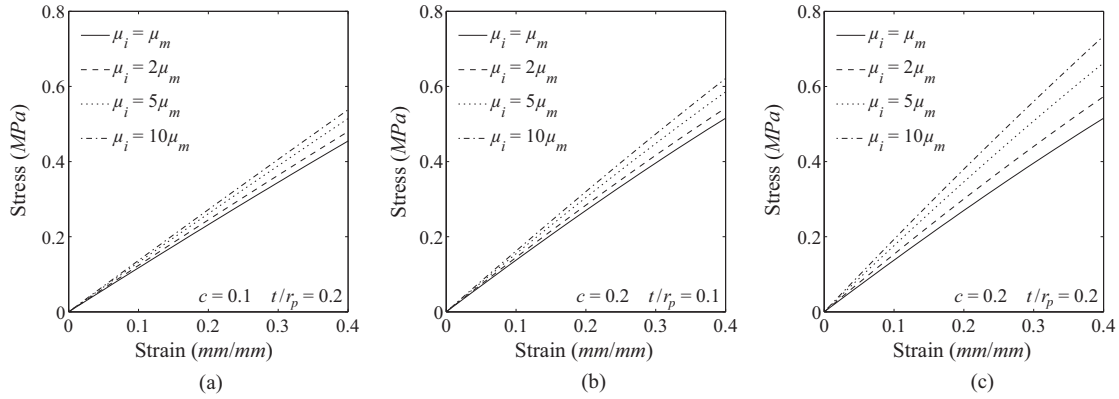


Fig. 21. Macroscopic constitutive response in simple shear for microstructures with: (a)  $c = 0.1$  and  $t/r_p = 0.2$ ; (b)  $c = 0.2$  and  $t/r_p = 0.1$ ; and (c)  $c = 0.2$  and  $t/r_p = 0.2$ .

the surface modification process of the silica particles. Two different surface treatments are considered, labeled as A-50 and UM-2.

The authors used a tensile tester, at room temperature, to determine the stress–strain curves, and used transmission electron microscopy (TEM) observations to determine the global effect of the different surface treatments. The authors report, through the use of swelling experiments, that the elastic properties of the rubber matrix were essentially unmodified for the A-50 treatment, but the crosslink density in the rubber increased with surface treatment UM-2. However, they provide no comments on the amount or type of bound rubber present in the composite. They concluded that the constitutive relation of the composite is significantly influenced by the interactions between the filler particles and the matrix. In some cases, they demonstrate that the surface treatment caused strong interfacial bonding between the inclusions and the rubber, however, in other cases the surface treatment resulted in weak bonding; which lead to interfacial debonding (or dewetting) of the particles at large strains. In the following, we will only consider the reported cases which involved interfacial debonding.

Additionally, the authors report the response of the unfilled rubber. Based on fitting the response of the rubber, we find an appropriate response of the rubber matrix, at least in uniaxial tension, follows the stored-energy function [49]:

$$W = \frac{3^{1-\alpha}}{2\alpha} \mu [I_1^\alpha - 3^\alpha]. \quad (19)$$

with material parameters  $\mu = 0.54$  and  $\alpha = 0.2$ , as illustrated in Fig. 22. As mentioned, for the surface treatment labeled as UM-2, the authors report that the amount of sulfur used in this treatment increased the crosslink density in the rubber. To account for this, we assume that this increases the effective modulus of the rubber, resulting in an increase in the shear modulus in the stored-energy function ( $\mu = 2.1$ ). The rubber is reinforced with a particle concentration of  $c_p = 0.26$ . Further, through a numerical investigation, we assume an interphase-thickness-to-particle-radius ratio of  $t/r = 0.2$ . Since the authors do not report the interphase stiffness, we select it here by fitting the numerical results to the experimental results. As illustrated in Fig. 22, for the A-50 treatment, an interphase modulus 3 times stiffer than that for the matrix,  $\mu_i = 3 \times \mu_m = 3 \times 0.54 \text{ MPa} = 1.62 \text{ MPa}$  leads to good agreement with the experimental results. Additionally, for the UM-2 treatment, an interphase modulus 2 times stiffer than that for the matrix,  $\mu_i = 2 \times \mu_m = 2 \times 2.1 \text{ MPa} = 4.2 \text{ MPa}$  leads to good agreement with the experimental results. As seen in Fig. 22, simulations of the same microstructures without the inclusion of interfacial debonding significantly overestimate the macroscopic constitutive response. The material properties used in the simulations are summarized in Table 1.

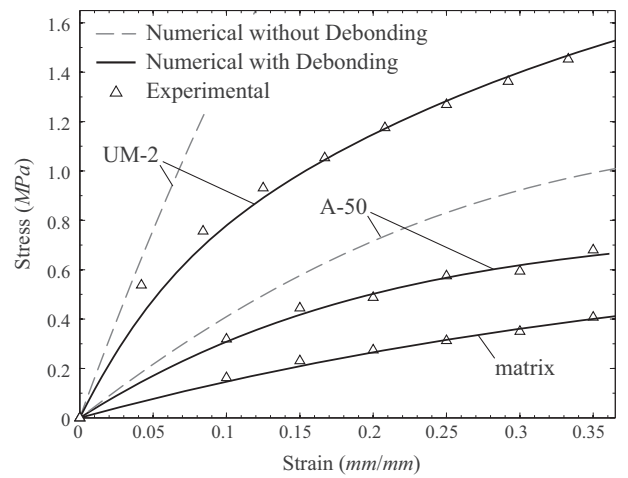


Fig. 22. Comparison of the proposed computational framework with experimental data.

Table 1

Summary of material properties used in the numerical comparison with experiments. The rate of transition between cohesive and friction forces is set at  $s = 3$ , in Eq. (15).

Treatment	Matrix modulus (MPa)	Interphase modulus (MPa)	Fracture energy (N/m)	Cohesive strength (MPa)	Coefficient of friction
A-50	0.54	1.62	1.0	0.5	1.0
UM-2	2.10	4.20	1.0	0.5	1.0

In summary, the above comparisons with experiments demonstrate that the proposed computational framework is able to provide an explanation for the varied macroscopic response of particle reinforced composites at finite deformations. Additionally, it confirms the significant influence of not only particle reinforcements, but also interfacial interactions on the constitutive response. Thus, in order to design these composites from the bottom up, it is not enough to only consider the influence of the particles, but one must also consider the influence of the interactions between the particles and the matrix. Finally, we note that, due to the necessity to make assumptions on the specific constituent properties not provided in the experiments, there are other potential combinations of constituent properties which may also be suitable at capturing the above described behavior. For example, the properties of the matrix may change in a different manner than we assumed, due to the use of the applied treatments, however, this does not negate the presence of interphases. And the

influence of the interphases compounds the influence of the changes in the matrix.

## 7. Concluding remarks

In this paper, we develop a computational framework to explore the influence of microscale features on the macroscale constitutive response of particle reinforced composites. While it has been shown experimentally that interphases significantly alter the macroscopic constitutive response of these composite materials, their inclusion in computational models of such composites is widely omitted. Through the use of representative unit cells, we demonstrate the influence of interphases and interfacial debonding on the global response of particle reinforced composites. We model interphases explicitly, and capture the interfacial debonding behavior of the particles, at large strains, using cohesive elements. To account for the frictional forces generated between each particle and its corresponding interphase, we developed a new, fully three-dimensional, coupled cohesive–friction constitutive relation. The use of this relation revealed that the consideration of friction in uniaxial tension can often be neglected, due to the small area of contact between the particles and the surrounding matrix. However, this is not the case when the microstructure experiences simple shear loading conditions; where we demonstrate that frictional forces can be significant, and should not be neglected. We validated the computational framework with experimental results from the literature which displayed both the presence of interphases and interfacial debonding. The comparison with experiments indicates that the proposed computational framework is able to provide an explanation for the varied macroscopic response of particle reinforced composites at finite deformations. Because of the challenges associated with experimentally obtaining the necessary measurements of material properties, a computational framework, such as the one presented in this paper, could prove helpful in shedding some light on the key parameters influencing the global response of this important class of materials.

In summary, this paper has been able to clearly demonstrate the significance of interphases and interfacial debonding on the macroscopic constitutive response of particle reinforced composites under large strains. However, there are many areas of this topic which lend themselves to being explored further. For example, the use of 80 particles to represent the polydisperse nature of the composite fixes the particle surface area, and thus, the frictional area of contact. If fewer particles or more particles were to be used to generate the same particle concentration, the surface area of the particles in contact with the matrix, and the resulting frictional forces, would change accordingly. Additionally, in this paper, we restrict our attention to spherical particles. The shape of the particles will likely influence the local stress field around the inclusion, so a potential extension of this work would be to consider alternative particle shapes. Ultimately, the goal would be to use experimental realizations of the microstructure to capture the precise locations and geometries of the particles and interphases. This could be done using the techniques of X-ray tomography or serial sectioning [50,51]. Finally, one could consider the influence of hysteretic loading on the global constitutive response.

## Acknowledgments

We acknowledge support from the Natural Sciences and Engineering Research Council of Canada and from the U.S. National Science Foundation through Grants #1321661 and #1437535. We also acknowledge support from the Raymond Allen Jones Chair at the Georgia Institute of Technology. The information presented in this publication is the sole opinion of the

authors and does not necessarily reflect the views of the sponsors or sponsoring agencies.

## Appendix A. Coupled material tangent stiffness matrix with friction

To incorporate the coupled cohesive and friction relations, many finite element codes require the implementation of a material tangent stiffness matrix,  $\mathbf{D}$ :

$$\mathbf{D} = \begin{bmatrix} D_{11} & D_{12} & D_{13} \\ D_{21} & D_{22} & D_{23} \\ D_{31} & D_{32} & D_{33} \end{bmatrix},$$

where the components of the stiffness matrix depend on the constitutive relation. Here, we list the components for any general coupled cohesive and any friction model:

$$D_{11} = \frac{\partial T_n}{\partial \Delta_n}, \quad D_{12} = \frac{\partial T_n}{\partial \Delta_t} \frac{\Delta_2}{\Delta_t}, \quad D_{13} = \frac{\partial T_n}{\partial \Delta_t} \frac{\Delta_3}{\Delta_t},$$

$$D_{21} = \frac{\partial T_t}{\partial \Delta_n} \frac{\Delta_2}{\Delta_t} + \frac{\partial T_f}{\partial \Delta_n} \frac{|\Delta_2|}{\Delta_t} \frac{\dot{\Delta}_2}{|\dot{\Delta}_2|},$$

$$D_{22} = \left( \frac{\partial T_t}{\partial \Delta_t} \Delta_2 + \frac{\partial T_f}{\partial \Delta_t} |\Delta_2| \frac{\dot{\Delta}_2}{|\dot{\Delta}_2|} \right) \frac{\Delta_2}{\Delta_t^2} + \left( T_t + T_f \frac{\Delta_2}{|\Delta_2|} \frac{\dot{\Delta}_2}{|\dot{\Delta}_2|} \right) \frac{\Delta_2^3}{\Delta_t^3},$$

$$D_{23} = \left( \frac{\partial T_t}{\partial \Delta_t} \Delta_2 + \frac{\partial T_f}{\partial \Delta_t} |\Delta_2| \frac{\dot{\Delta}_2}{|\dot{\Delta}_2|} \right) \frac{\Delta_3}{\Delta_t^2} - \left( T_t \Delta_2 + T_f |\Delta_2| \frac{\dot{\Delta}_2}{|\dot{\Delta}_2|} \right) \frac{\Delta_3}{\Delta_t^3},$$

$$D_{31} = \frac{\partial T_t}{\partial \Delta_n} \frac{\Delta_3}{\Delta_t} + \frac{\partial T_f}{\partial \Delta_n} \frac{|\Delta_3|}{\Delta_t} \frac{\dot{\Delta}_3}{|\dot{\Delta}_3|},$$

$$D_{32} = \left( \frac{\partial T_t}{\partial \Delta_t} \Delta_3 + \frac{\partial T_f}{\partial \Delta_t} |\Delta_3| \frac{\dot{\Delta}_3}{|\dot{\Delta}_3|} \right) \frac{\Delta_2}{\Delta_t^2} - \left( T_t \Delta_3 + T_f |\Delta_3| \frac{\dot{\Delta}_3}{|\dot{\Delta}_3|} \right) \frac{\Delta_2}{\Delta_t^3},$$

$$D_{33} = \left( \frac{\partial T_t}{\partial \Delta_t} \Delta_3 + \frac{\partial T_f}{\partial \Delta_t} |\Delta_3| \frac{\dot{\Delta}_3}{|\dot{\Delta}_3|} \right) \frac{\Delta_3}{\Delta_t^2} + \left( T_t + T_f \frac{\Delta_3}{|\Delta_3|} \frac{\dot{\Delta}_3}{|\dot{\Delta}_3|} \right) \frac{\Delta_3^2}{\Delta_t^3}.$$

For the specific friction model presented in this paper:

$$\frac{\partial T_f}{\partial \Delta_n} = \left( 1 - \frac{T_t(0, \Delta_t)}{D_0 \Delta_t} \right)^s \mu \frac{T_n}{|T_n|} \frac{\partial T_n}{\partial \Delta_n}, \quad \text{and}$$

$$\frac{\partial T_f}{\partial \Delta_t} = s \left( 1 - \frac{T_t(0, \Delta_t)}{D_0 \Delta_t} \right)^{s-1} \mu |T_n| \left( \frac{T_t(0, \Delta_t)}{D_0 \Delta_t^2} - \frac{\partial T_t(0, \Delta_t)}{\partial \Delta_t} \frac{1}{D_0 \Delta_t} \right).$$

The partial derivatives  $\left( \frac{\partial T_n}{\partial \Delta_n}, \frac{\partial T_n}{\partial \Delta_t}, \frac{\partial T_t}{\partial \Delta_n}, \text{ and } \frac{\partial T_t}{\partial \Delta_t} \right)$  for the PPR cohesive model are not listed here, but are published elsewhere [52,38].

## Appendix B. Example: activation of friction in a masonry wallette

Since the coupled cohesive–friction model presented in this paper is new, and the particular application under investigation in this paper shows little influence due to friction (see Section 5.2.1), a supplementary example is selected to provide further support to the model. This supplementary example considers the shear loading of a masonry wallette. This example

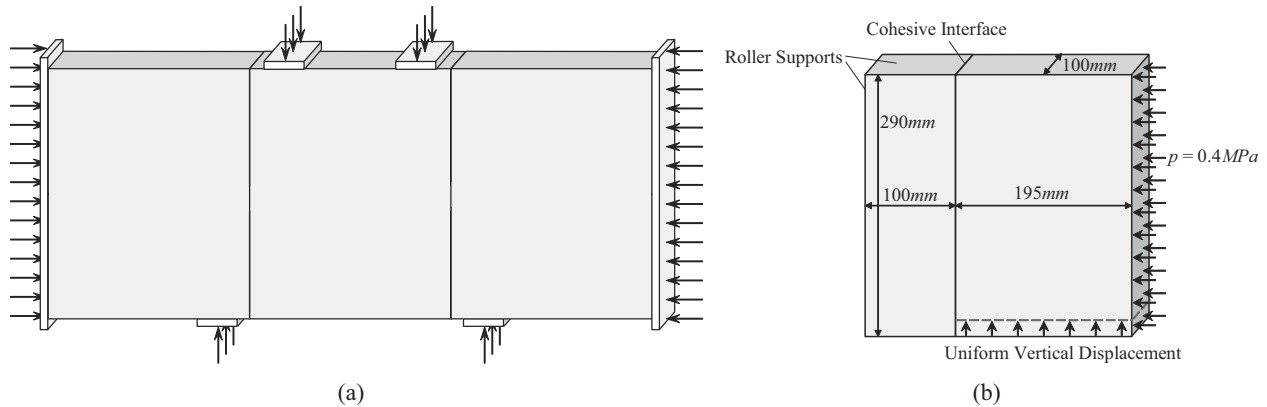


Fig. B.23. Model of a masonry wallette: (a) full model, based on experimental setup and (b) numerical model used in simulations.

Table B.2

Summary of cohesive properties used for the interface elements.

Fracture energy ( $\phi_t$ )	Cohesive strength ( $\tau$ )	Softening parameter ( $\beta$ )	Penalty stiffness ( $\lambda_t$ )	Coefficient of friction ( $\mu$ )
750 N/m	0.45 MPa	5	0.04	0.77

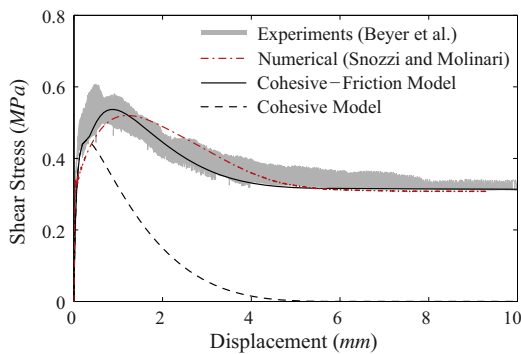


Fig. B.24. Shear stress plotted as a function of applied displacement for the masonry wallette example. The experimental data is extracted from Beyer et al. [53], and the numerical results from Snozzi and Molinari [42] are included for comparison.

demonstrates the influence of the coupled cohesive–friction model when a significant frictional effect is activated. The masonry wallette consists of three bricks, linked with two mortar joints, as illustrated in Fig. B.23(a). During the experimental testing [53], the middle brick is supported at its top edge by two rigid blocks, and a shear load is introduced through an applied displacement on the lower edge of the outer two bricks. The vertical edges of the wallette are loaded by two load cells which control the horizontally applied pressure. The experimental investigation of this wallette was conducted by Beyer et al. [54,53].

This problem has also been investigated numerically by Snozzi and Molinari [42]. They modeled this problem with a dynamic fracture code and adaptively inserted cohesive elements at the interface. In their simulations they used material damping to reduce the oscillations they observed in their results. Numerically, the model uses symmetric boundary conditions and only considers half the full model, as illustrated in Fig. B.23(b). The domain is discretized using a uniform mesh of linear brick elements of dimension  $5 \times 5 \times 5$  mm. The resulting discretization contains 68,400 elements and 75,579 nodes. Moreover, 3500 cohesive elements

are used to capture the failure/friction response of the interface. The bricks have an elastic modulus of 14.0 GPa, and a Poisson's ratio of 0.15. The properties of the cohesive interface are listed in Table B.2. The lower boundary of the outer brick is displaced vertically, and, as in the testing machine, the specimen is loaded with an imposed horizontal displacement with a constant normal pressure level of 0.4 MPa.

To determine the influence of frictional forces on the global response, we consider cases with and without friction included in the model. The results from our investigation are illustrated in Fig. B.24. The shear force is calculated as the applied force on the lower surface of the outer brick divided by the area of the interface between the two bricks. The experimental data from Beyer et al. [53] is included for comparison. The numerical results including the presence of friction demonstrate good agreement with the response observed experimentally. Initially, the stiffness of the composite increases in accordance with the response of the bricks. After cohesive softening initiates, the response transitions smoothly to a purely frictional regime; which the model is able to accurately capture. When friction effects are not included in the model, the shear stress follows the cohesive model and transitions to zero stress at a finite displacement; which is inconsistent with the response obtained experimentally.

## References

- [1] J.L. Leblanc, *Prog. Polym. Sci.* 27 (2002) 627–687.
- [2] J.L. Leblanc, *Filled Polymers: Science and Industrial Applications*, CRC Press, 2010.
- [3] Y. Qiao, *Scr. Mater.* 49 (2003) 491–496.
- [4] J. Segurado, J. Llorca, *Int. J. Solids Struct.* 41 (2004) 2977–2993.
- [5] R. Kitey, H. Tippur, *Acta Mater.* 53 (2005) 4.
- [6] J. Ramier, *Comportement mécanique d'élastomères chargés, influence de l'adhésion charge – polymère, influence de la morphologie*, Ph.D. Thesis, L'Institut National des Sciences Appliquées de Lyon, 2004.
- [7] N. Suzuki, M. Ito, F. Yatsuyanagi, *Polymer* 46 (2005) 193–201.
- [8] J. Ramier, L. Chazeau, C. Gauthier, *Rubber Chem. Technol.* 80 (2007) 183–193.
- [9] F. Yatsuyanagi, N. Suzuki, M. Ito, H. Kaidou, *Polym. J.* 34 (2002) 332–339.
- [10] M. Qu, J.S. Meth, G.S. Blackman, G.M. Cohen, K. Sharp, K.J. Van Vliet, *Soft Matter* 7 (2011) 8401–8408.
- [11] M. Qu, F. Deng, S.M. Kalkhoran, A. Gouldstone, A. Robisson, K.J. Van Vliet, *Soft Matter* 7 (2011) 1066–1077.
- [12] B. Wetzel, P. Rosso, F. Hauptert, K. Friedrich, *Eng. Fract. Mech.* 73 (2006) 2375–2398.
- [13] Y.S. Thio, A.S. Argon, R.E. Cohen, *Polymer* 45 (2004) 3139–3147.
- [14] A.N. Gent, B. Park, *J. Mater. Sci.* 19 (1984) 1947–1956.
- [15] A.V. Zhuk, N.N. Knunyants, V.G. Oshmyan, V.A. Topolkarayev, A.A. Berlin, *J. Mater. Sci.* 28 (1993) 4595–4606.
- [16] L. Brassart, H.M. Inglis, L. Delannay, I. Doghri, P.H. Geubelle, *Comput. Mater. Sci.* 45 (2009) 611–616.
- [17] T. Mori, K. Tanaka, *Acta Metall.* 21 (1973) 571–574.
- [18] T. Goudarzi, D.W. Spring, G.H. Paulino, O. Lopez-Pamies, *J. Mech. Phys. Solids* 80 (2015) 37–67.
- [19] A. Needleman, *ASME J. Appl. Mech.* 54 (1987) 525–531.

- [20] K. Park, G.H. Paulino, *Appl. Mech. Rev.* 64 (2013) 1–20.
- [21] X.A. Zhong, W.G. Knauss, *J. Eng. Mater. Technol.* 119 (1997) 198–204.
- [22] X.A. Zhong, W.G. Knauss, *Mech. Compos. Mater. Struct.* 7 (2000) 35–53.
- [23] J. Moraleda, J. Segurado, J. Llorca, *Int. J. Solids Struct.* 46 (2009) 4287–4297.
- [24] H.M. Inglis, P.H. Geubelle, K. Matouš, H. Tan, Y. Huang, *Mech. Mater.* 39 (2007) 580–595.
- [25] K. Matouš, P.H. Geubelle, *Int. J. Numer. Methods Eng.* 65 (2006) 190–223.
- [26] K. Matouš, P.H. Geubelle, *Comput. Methods Appl. Mech. Eng.* 196 (2006) 620–633.
- [27] O. Lopez-Pamies, T. Goudarzi, K. Danas, *J. Mech. Phys. Solids* 61 (2013) 19–37.
- [28] J. Schröberl, *Comput. Visualization Sci.* 1 (1997) 41–52.
- [29] W.J. Drugan, J.R. Willis, *J. Mech. Phys. Solids* 44 (1996) 497–524.
- [30] Z. Khisaeva, M. Ostoja-Starzewski, *J. Elasticity* 85 (2006) 153–173.
- [31] J. Segurado, J. Llorca, *J. Mech. Phys. Solids* 50 (2002) 2107–2121.
- [32] Abaqus, Version 6.11 Documentation, 2011. Dassault Systemes Simulia Corp. Providence, RI, USA.
- [33] O. Pierard, C. González, J. Segurado, J. Llorca, I. Doghri, *Int. J. Solids Struct.* 44 (2007) 6945–6962.
- [34] Z. Guo, X. Shi, Y. Chen, H. Chen, X. Peng, P. Harrison, *Mech. Mater.* 70 (2014) 1–17.
- [35] X.P. Xu, A. Needleman, *Model. Simul. Mater. Sci. Eng.* 1 (1993) 111–132.
- [36] M. Ortiz, A. Pandolfi, *Int. J. Numer. Methods Eng.* 44 (1999) 1267–1282.
- [37] K. Park, G.H. Paulino, J.R. Roesler, *J. Mech. Phys. Solids* 57 (2009) 891–908.
- [38] D.W. Spring, G.H. Paulino, *Eng. Fract. Mech.* 126 (2014) 190–216.
- [39] A. Pandolfi, P.R. Guduru, M. Ortiz, A.J. Rosakis, *Int. J. Solids Struct.* 37 (2000) 3733–3760.
- [40] V. Tomar, J. Zhai, M. Zhou, *Int. J. Numer. Methods Eng.* 61 (2004) 1894–1920.
- [41] H.D. Espinosa, S. Dwivedi, H.-C. Lu, *Comput. Methods Appl. Mech. Eng.* 183 (2000) 259–290.
- [42] L. Snozzi, J.F. Molinari, *Int. J. Numer. Methods Eng.* 93 (2013) 510–526.
- [43] V. Tvergaard, *Mater. Sci. Eng. A* 125 (1990) 203–213.
- [44] J.L. Chaboche, R. Girard, A. Schaff, *Comput. Mech.* 20 (1997) 3–11.
- [45] V. Acary, Y. Monerie, Nonsmooth fracture dynamics using a cohesive zone approach, Tech. rep., Institut National de Recherche en Informatique et en Automatique, 2006.
- [46] G. Alfano, E. Sacco, *Int. J. Numer. Methods Eng.* 68 (2006) 542–582.
- [47] R.W. Ogden, *Nonlinear Elastic Deformations*, Courier Dover Publications, 1997.
- [48] T. Goudarzi, O. Lopez-Pamies, *J. Appl. Mech.* 80 (2013) 050906-1–050906-10.
- [49] O. Lopez-Pamies, *C.R. Mec.* 338 (2010) 3–11.
- [50] Z. Shan, A.M. Gokhale, *Acta Mater.* 49 (2001) 2001–2015.
- [51] J.J. Williams, J. Segurado, J. Llorca, N. Chawla, *Mater. Sci. Eng.: A* 557 (2012) 113–118.
- [52] K. Park, G.H. Paulino, *Eng. Fract. Mech.* 93 (2012) 239–262.
- [53] K. Beyer, A. Dazio, *Earthq. Spectr.* 28 (2012) 885–906.
- [54] K. Beyer, A. Abo-El-Ezz, A. Dazio, Quasi-static cyclic tests on different types of masonry spandrels, Tech. rep., Report No 327, Institute of Structural Engineering, Swiss Federal Institute of Technology Zürich, 2010.